# Argon and Xenon Plasma Energy Analysis in a Pulsed Inductive Test Article

**IEPC-2013-362**

*Presented at the 33$^{rd}$ International Electric Propulsion Conference,*
*The George Washington University, Washington, D.C., USA*
*October 6–10, 2013*

Ryan A. Pahl* and Joshua L. Rovey†
*Missouri University of Science and Technology, Rolla, MO, 65401, USA*

**Abstract: Energy distribution results from pulsed inductive discharges in Argon and Xenon are presented. Calculations are based on a series RLC circuit analysis of the Missouri Plasmoid Experiment in vacuum and plasma. Initial results show an energy deficit of 16.3 J and 15.9 J for Argon and Xenon, respectfully, for a 10 mTorr pre-fill with 79.5 J initial stored energy. At 100 mTorr, the deficits increased to 21.1 J and 21.6 J, respectfully. Magnetic field topography is measured using an array of eleven $\dot{B}$ probes distributed uniformly over the longitudinal axis. A peak vacuum magnetic field of 36.2 mT is observed. Increases in magnetic field magnitude as high as 36.2% is observed near the wall after plasma formation.**

## Nomenclature

$A$ = area [m$^2$]
$\dot{B}$ = magnetic field [T]
$C$ = capacitance [F]
$E$ = energy [J]
$I$ = current [A]
$I_{sp}$ = specific impulse [s]
$l$ = length [m]
$L$ = inductance [H]
$m_e$ = mass of an electron [kg]
$\mu_0$ = permeability of free space [H·m$^{-1}$]
$n$ = number of turns
$q$ = elementary charge [C]
$R$ = resistance [Ω]
$r_g$ = gyroradius [m]
$t, \tau$ = time [s]
$V$ = voltage [V]
$v_\perp$ = perpendicular velocity [m/s]
$\mathcal{V}$ = volume [m$^3$]
$\omega$ = angular frequency [s$^{-1}$]

*Graduate Student, Mechanical and Aerospace Engineering, rap4yd@mst.edu, Toomey Hall, 400 W. 13th St., Rolla, MO, 65409-0500, and AIAA Student Member.
†Assistant Professor, Mechanical and Aerospace Engineering, roveyj@mst.edu, Toomey Hall, 400 W. 13th St., Rolla, MO, 65409-0500, and AIAA Senior Member.

# I. Introduction

PULSED inductive plasma (PIP) devices have garnered much attention in recent years in the fusion and spacecraft communities.[1–7] Recent tests on the Magnetically Accelerated Plasmoid (MAP) thruster have achieved an $I_{sp}$ of 18-20 ks at 70 MW (continuous operation) using deuterium. An optimization analysis yields an $I_{sp}$ of 6-8 ks at 10 MW (20 kHz) with an estimated system efficiency of 70-80%.[6] Results from the ELF thruster show $I_{sp}$'s of 1-6 ks for the heavier gases: Nitrogen, Air, and Xenon. Despite these and other successes, the energy conversion process during early plasma formation is not well understood. In these pulsed systems, energy is initially stored as electrical energy in capacitor banks. During discharge, this energy is converted to electrical and magnetic fields to breakdown a neutral gas and accelerate the resulting plasma to high velocity. This paper presents the preliminary results from an energy coupling analysis of Argon and Xenon gases in a ringing theta pinch configuration. The distribution of energy as a function of time is presented for the vacuum and plasma cases over pressures ranging from 10 - 100 mTorr.

# II. Experimental Setup

To study the energy mechanisms associated with heavy-gas PIP devices, a series of tests were conducted using Argon and Xenon at different fill pressures. Fill pressures tested were from zero to 100 mTorr in ten mTorr increments. This section details the experiment setup and diagnostics used to obtain the data presented in this paper.

## A. Missouri Plasmoid Experiment

The Missouri Plasmoid Experiment (MPX) is a pulsed-inductive test article located at the Aerospace Plasma Laboratory at Missouri S&T. MPX consists of a high-voltage capacitor and an eleven-segment theta pinch coil. Each segment of the theta pinch coil is constructed from aluminum 7075 and consists of two identical segment halves which are bolted together during assembly using two 0.95 cm threaded rods. The resulting segment has a diameter of 17.8 cm and a thickness of 6.67 cm. The eleven segments are mounted horizontally and connected with four 1.27 cm threaded rods. Nylon spacers machined to a 5.0 mm thickness are inserted between coil segments to allow for axial relief of magnetic diagnostics. The total length of the assembled theta pinch coil is 78.35 cm. Aluminum plates measuring 78.35 cm x 12.7 cm x 0.64 cm are bolted to the theta pinch coil to provide an interface for integrating the theta pinch coil into the remaining MPX components. Four bolts per segment are used to attach the aluminum plates to the theta pinch coil to reduce the joint resistance and inductance.

A grade 214 quartz tube is placed inside the theta pinch coil and serves as the vacuum vessel for plasma formation. The quartz tube has a inner and outer diameter of 15.5 and 16.1 cm, respectfully, and a length of 90 cm. Acrylic plates are located at both ends of the theta pinch coil to ensure the quartz tube remains aligned with the theta pinch coil. The south end of the quartz tube is mated to the Missouri S&T vacuum facility[8] using a Duniway VBJG-7 L-gasket. An aluminum flange is mated to the north end of the quartz tube using an identical L-gasket. Gas inlet and pressure gauge ports are located on the north end aluminum flange. A MKS model 626 Baratron pressure gauge is used to measure fill pressures in MPX and is designed for pressures ranging from 0.01 - 100 mTorr.

A 0.707 F capacitor is positioned approximately 20 cm from the edge of the theta pinch coil. The Maxwell 33934 capacitor is rated for 70 kV and has a series inductance of 50 nH. A Excelitas GP-12B spark gap and TR-1700 trigger transformer are used to initiate the discharge of MPX. The adjacent electrode is connected to the anode of the capacitor and the opposite electrode is connected to the theta pinch coil using a copper busbar. A second copper busbar is used to connect the capacitor cathode to the theta pinch coil. A tungsten electrode is inserted on the south flange and connected to a high voltage supply. This pre-ionization (PI) stage is set to 1.7 kV and provides seed electrons to assist the breakdown process. The fully integrated MPX system is shown in Fig. 1. More information regarding the triggering system can be found in Ref. 8.

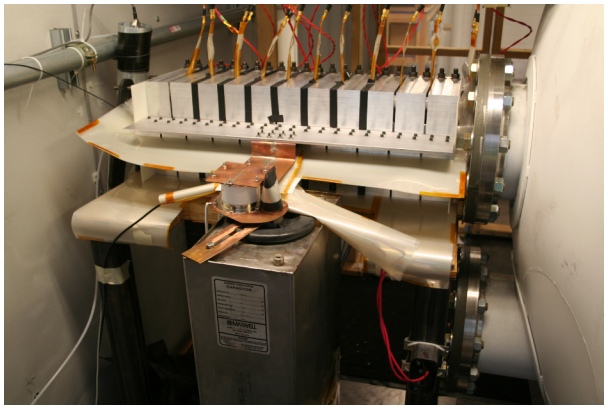

Figure 1: Missouri Plasmoid Experiment (MPX) connected to Aerospace Plasma Laboratory vacuum facility.

### B. Diagnostics

#### 1. *Magnetic Probes*

A Pearson 4418 current monitor is used to measure the total discharge current of MPX. An acrylic insert is press-fit into the center of the current monitor to provide high voltage insulation and ensure the current monitor remains centered about the capacitor cathode. All probes use a 50 Ω termination to minimize noise.

An array of $\dot{B}$ probes are used to measure the axial magnetic field during an experiment discharge. The custom differential $\dot{B}$ probe design uses two Coilcraft 1008CS-102XFLB surface mount inductors on a small PCB. Probe leads are constructed of low-profile 3.58 mm OD semi-rigid coax soldered to SMA connectors. Details of the probe construction and calibration can be found in Ref. 9. An acrylic probe holder spans the axial length of the quartz tube and machined rectangular slots align a probe under the center of each coil segment. The probe locations as measured from the center of the theta pinch coil are: 0.00, ±7.2, ±14.3, ±21.5, ±28.7, and ±35.8 cm. $\dot{B}$ probe 1 is located at -35.8 cm on the north end of MPX and probe 11 is located at 35.84 cm on the south end of MPX. Probe leads run axially a short distance under the coil segment and then exit the theta coil through the gap between segments. The probe leads are connected to 1.22 m of RG-400 coax cable that runs into a shielded conduit. Once in the shielded conduit, the RG-400 cable transitions to 6.63 m of RG-223 coax cable. Two Bird 25-A-MFN-10 attenuators in series provide a 20 dB attenuation. An additional 1.83 m of RG-223 cable connects the attenuator pair to a National Instruments PXI-1000B chassis. All data are collected using four PXI-5105 12-bit digitizers allowing for a total of 32 channels of data acquisition.

## III. Results

This section presents the current and magnetic results obtained from MPX testing with Argon and Xenon. The results for the vacuum, 10, 30, 50, and 100 mTorr cases are presented. Each parameter set in the testing matrix has been replicated five times and the results averaged and presented below.

### A. Current Monitor

The Pearson 4418 current monitor measures the time-varying discharge current of MPX. In the vacuum case, a maximum current of 27.2 kA is measured. Tests with Argon yielded a maximum current of 28.0 kA at 30 mTorr while Xenon had a maximum current of 28.0 kA at 10 mTorr. To analyze the current profile in frequency domain, a fast-Fourier transform (FFT) is used. The primary discharge frequency for the vacuum and plasma tests are 443 kHz and 466 kHz, respectfully. This variation in discharge frequency is illustrated in time domain in Fig. 2a and in frequency domain in Fig. 2b.

The 5.3% increase in discharge frequency is combined with an increased dampening ratio resulting in a reduced number of current oscillations before returning to a quiescent state. Furthermore, the presence of plasma smooths the resulting current waveform resulting in a clearly defined peak. The vacuum case still has considerable noise resulting in a slightly ambiguous waveform peak.

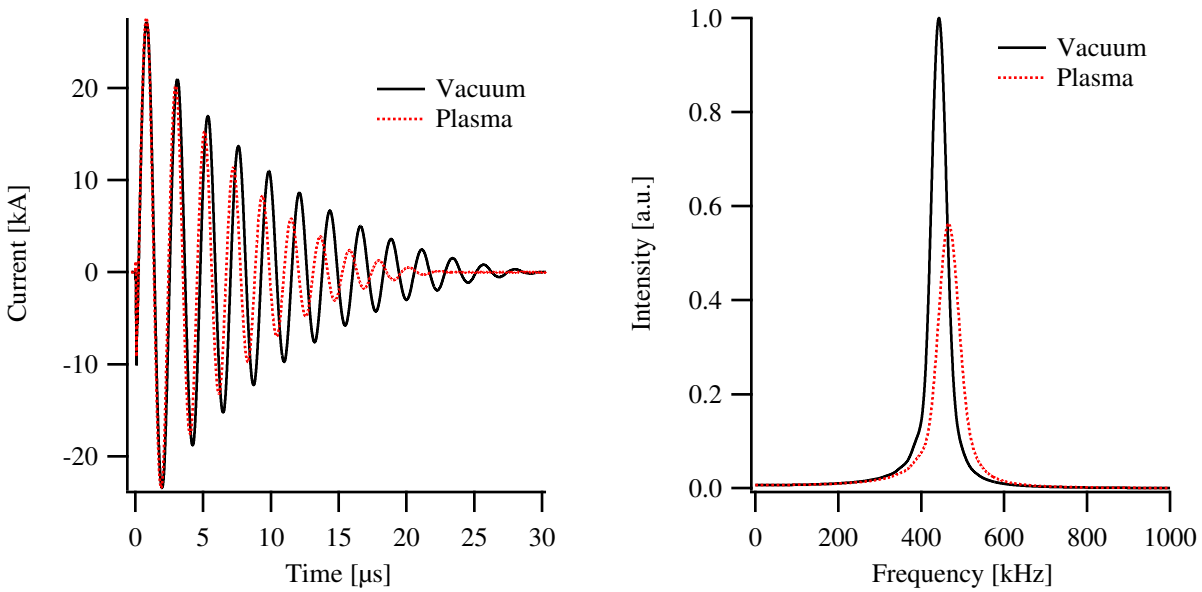


(a) Time Domain

(b) Frequency Domain

Figure 2: MPX discharge current measured with Pearson 4418 current monitor. Plasma test taken with a 10 mTorr Argon pre-fill.

Additionally, rather than having a single discharge frequency, a clear broadening in the frequency domain is observed in both the vacuum and plasma cases. When plasma is present, the peak intensity of the FFT is reduced to 56% of the vacuum peak intensity and has a full-width half-max of 62.0 kHz compared to 44.9 kHz for the vacuum case, an increase of 44%.

### B. $\dot{B}$ Probes

Sample data sets of $\dot{B}$ data taken in vacuum and 10 mTorr Argon pre-fill are illustrated for probes 1 and 6 in Figs. 3a and 3b, respectfully. As observed in the discharge current, the formation of plasma results in an increasing discharge frequency and reduced oscillation cycles. However, the presence of plasma results in a distinctly different trend in the time-varying magnetic field. A clear deviation from the vacuum case is evident just prior to the first trough at approximately 0.41 $\mu$s after discharge. As a result, significant variations in the first few current waveform troughs are observed. A small increase of 1.6% is observed in the plasma test peak current compared to the vacuum test. This small difference is reflected in the near identical peaks in the vacuum and plasma $\dot{B}$ waveforms. Despite the similar peak values, the first trough of $\dot{B}$ probe 1 records a 15.7% reduction in plasma $\dot{B}$ magnitude, a decrease of 3.3% at the second peak, and an increase of 6.5% on the second trough. The trend observed at the center of the coil by $\dot{B}$ probe 6 varies significantly. An increase of 27.3% in the plasma $\dot{B}$ signal is observed at the first trough, an increase of 33.8% at the second peak, and an increase of 28.9% on the second trough.

## IV. Analysis and Discussion

In this section, the measured magnetic field values are compared to solenoid theory. Furthermore, contour plots of the magnetic field show the time evolution of the magnetic field within the theta pinch coil. Additionally, an energy analysis of the MPX system is performed to quantify the effect of plasma formation on the energy present in the MPX system. An RLC simulation using a least squares error (LSE) is used to determine the total series inductance of the MPX system. The energy stored in the capacitor, system inductance, theta pinch coil, and ohmic heating are analyzed for Argon and Xenon at selected pressures and presented.

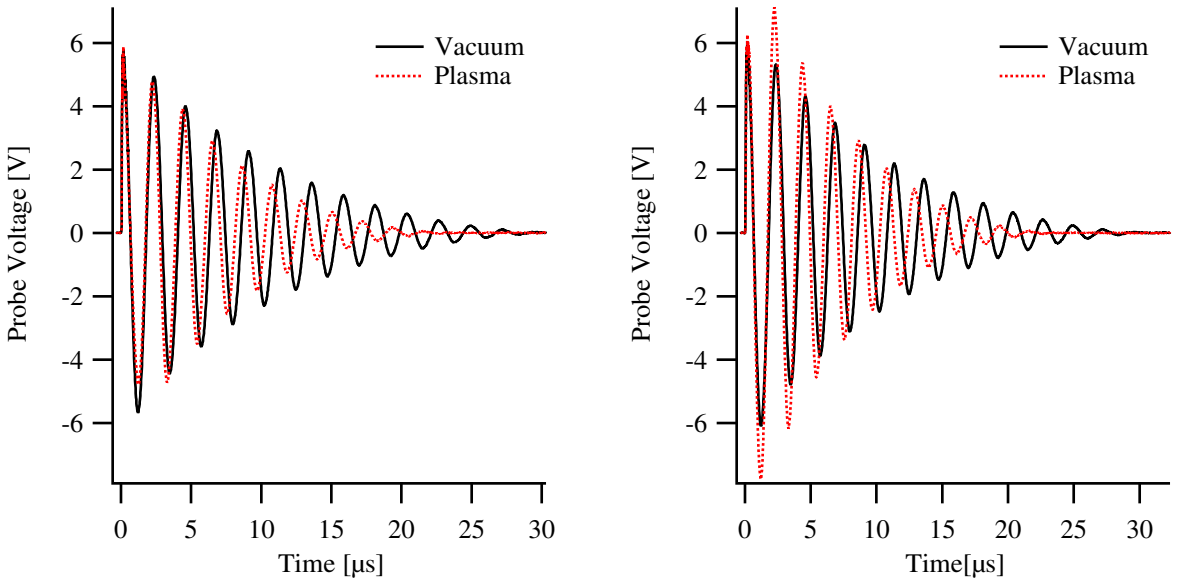


(a) $\dot{B}$ probe 1 (b) $\dot{B}$ probe 6

Figure 3: $\dot{B}$ probe voltage measured at the end (probe 1) and center (probe 6) of the theta pinch coil. Plasma test conducted with a 10 mTorr pre-fill of Argon.

### A. Magnetic Field

The voltage recorded by the $\dot{B}$ probes is directly proportional to the time rate of change of the magnetic field as given by Faraday's equation:

$$V(t)_{probe} = nA(\omega)\frac{dB(t)}{dt}, \tag{1}$$

where $n$ is the number of loops on the $\dot{B}$ probe and $A$ is the effective cross-sectional area of the $\dot{B}$ probe. The magnetic field can then be found by integrating the probe signal with respect to time as show in Eq. 2.

$$B(t) = \frac{1}{nA(\omega)}\int_0^t V(\tau)_{probe}d\tau \tag{2}$$

While the physical area of the probe does not change, the inductance of the probe has a complex impedance that increases with frequency. The probe impedance increases with frequency resulting in reduced probe output voltage. The concept of an effective probe area captures this concept. As frequency increases, the effective area of the probe is said to decrease which accounts for the reduced probe voltage. Once the effective area is determined for the frequencies of interest, the magnetic field can be calculated. The design and calibration of $\dot{B}$ probes is not a trivial task and numerous authors have contributed to this task.[10–17] C. Hill[18] offers a very detailed analysis of complex impedance considerations of $\dot{B}$ probes and methods of probe calibration for use in field reversed configuration (FRC) plasmas. The calibration method used for the MPX $\dot{B}$ probes can be found in Ref. 9. Sample data sets of integrated $\dot{B}$ data taken in vacuum and 10 mTorr Argon pre-fill are illustrated for probes 1 and 6 in Figs. 4a and 4b, respectfully. The magnetic field measured by probe 1 shows a 8.3% reduction in field magnitude at the first peak and 37.2% at the first trough. The second peak experiences a field magnitude increase of 6.0%. At the center of the coil, probe 6 shows that the magnetic field increase 5.6% at the first peak, 36.2% at the first trough, and 1.3% at the second peak. For both probes, the magnetic field appears to return to a the standard underdamped waveform observed in the vacuum case after the fourth peak. The relatively small deviations in field magnitude observed in the first peak indicates minimal plasma effects on the first quarter cycle of the discharge. In both cases, the largest field deviations occur at the first trough and show more than 133% of the vacuum magnetic field. This indicates that the primary plasma formation occurs prior to the three-quarters cycle but after

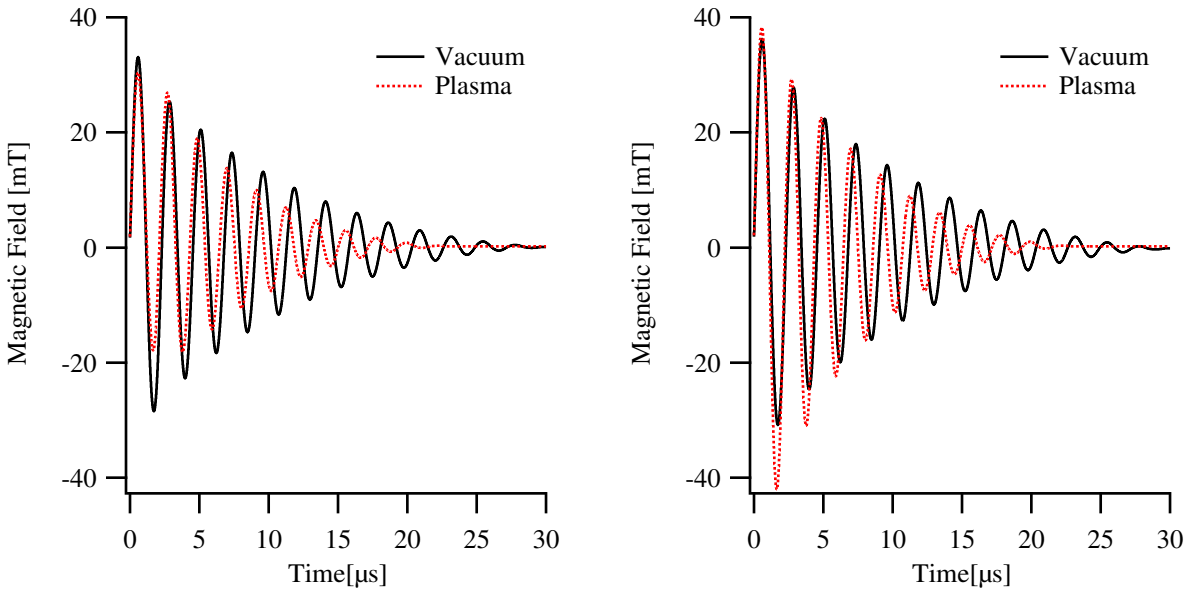


(a) $\dot{B}$ probe 1 (b) $\dot{B}$ probe 6

Figure 4: Time-varying magnetic field measured at the end (probe 1) and center (probe 6) of the theta pinch coil. Plasma test conducted with a 10 mTorr pre-fill of Argon.

the quarter cycle. This is in agreement with the literature[3,4,19] that indicates plasma formation occurs after the magnetic field crosses the null region and is realized from the equation of electron gyroradius,

$$r_g = \frac{m_e v_\perp}{|q|B}, \tag{3}$$

where $m_e$ is the mass of an electron, $v_\perp$ is the velocity perpendicular to the magnetic field, and $q$ is the charge of an electron. As the first quarter cycle is approached, the gyroradius starts to increase as the magnetic field approaches zero. Increasing the gyroradius increases the probability of collisions which leads to a greater number of ionized particles. Conversely, without the confining effects of the magnetic field, electron transport to the walls increases removing energy from the system.

The time evolution of the magnetic field of Argon and Xenon for vacuum, 10, 30, 50, and 100 mTorr pre-fills are presented in Figs. 5 and 6, respectfully. The vacuum tests were repeated after replacing gas bottles and provide a metric for comparing the operation of MPX pre and post gas change. The vacuum tests for Argon and Xenon show near identical profiles indicating a high degree of consistency in field topography. The bow tie shape observed in the vacuum case illustrates the slight magnetic mirror formed when current pools at the ends of the theta pinch coil during discharge. A field aberration is observed at 5.1 $\mu$s and 11.9 $\mu$s where the field shows increased magnitude at 35.84 cm. This is likely due to the presence of the PI stage present on that end of the theta pinch coil. After 11.9 $\mu$s, the field topography no longer shows axial variations in magnetic field.

Plasma occurs at 10 mTorr for both Argon and Xenon. The presence of plasma alters the field topography, replacing the bow tie pattern with a more elliptical geometry. The exception to this occurs at 2.9 $\mu$s for all pressures in both gases where the bow tie pattern is still observed. In the 10 mTorr case, the peak magnetic field for Xenon is 3.4% larger than Argon but Argon shows a 0.8% larger field magnitude at 1.6 $\mu$s. This trend of Xenon showing larger field magnitudes during $\frac{1}{4}n$ quarter cycles and Argon dominating at the $\frac{3}{4}n$ quarter cycles persists until 9.1 $\mu$s where Argon then consistently has the largest field magnitudes. However, after five $\mu$s, the variations in field magnitudes between the gases is negligible. Compared to the vacuum case, Xenon and Argon experience increased field magnitudes at the $\frac{1}{4}$ cycle of 9.4% and 5.7%, respectfully, and 35.1% and 36.2%, respectfully, at the $\frac{3}{4}$ cycle.

The largest variations between Argon and Xenon occur at 30 mTorr. The magnetic field magnitude for Xenon exceeds that of Argon at the first trough and peak by 5.9% and 6.8%, respectfully. Compared to the

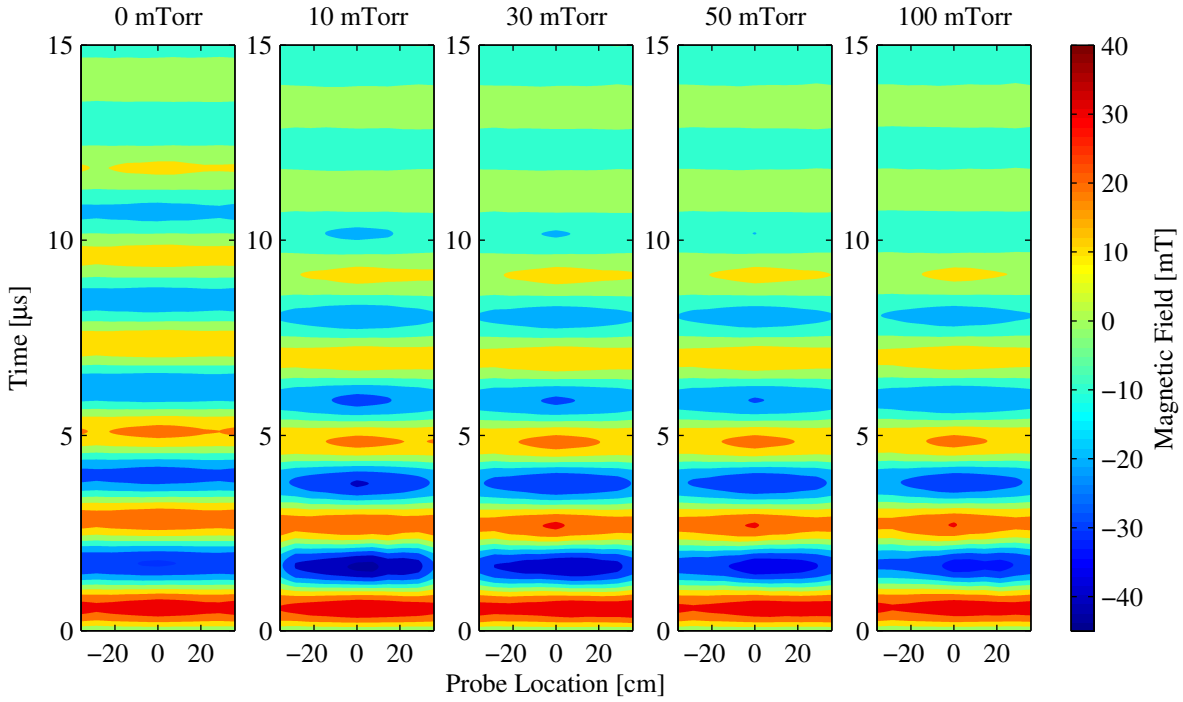


Figure 5: Contour plot showing MPX magnetic field topography temporal evolution for Argon at multiple pressures.

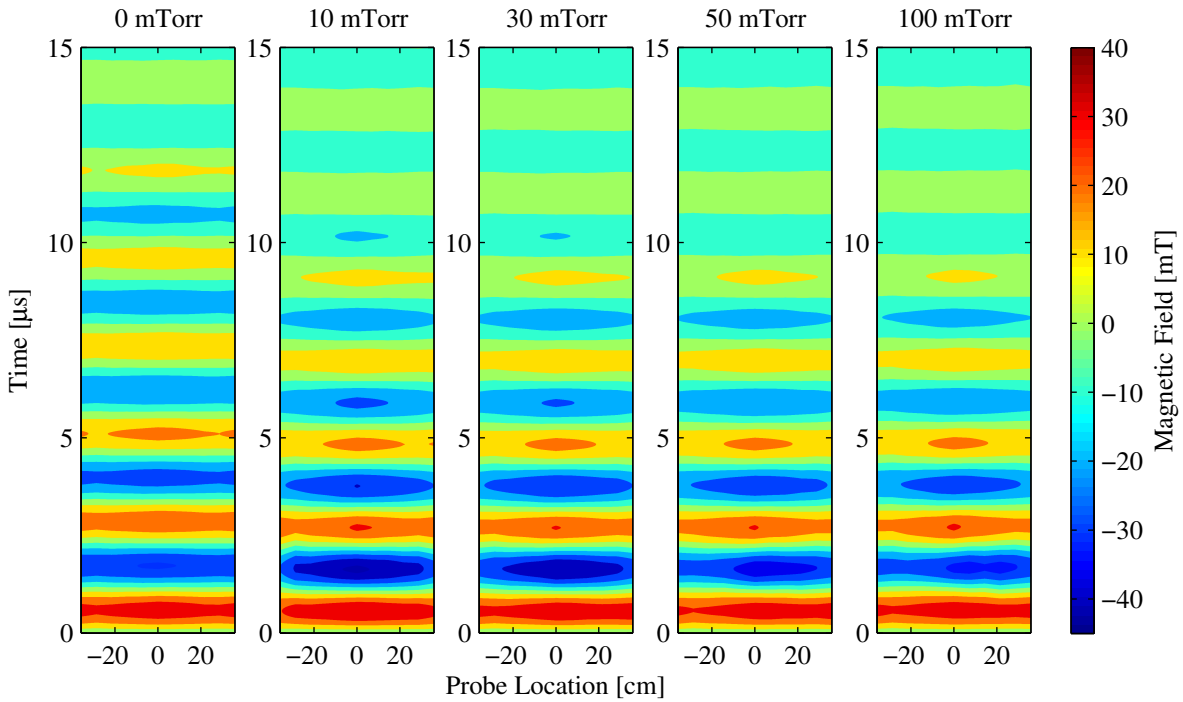


Figure 6: Contour plot showing MPX magnetic field topography temporal evolution for Xenon at multiple pressures.

vacuum case, the magnetic field of Xenon increased by 6.1% at the $\frac{1}{4}$ cycle where Argon decreased by 0.2%. At the $\frac{3}{4}$ cycle, Xenon and Argon experienced an increase of 31.8% and 23.0%, respectfully. Relative to 10 mTorr, at the first $\frac{1}{4}$ cycle, Xenon and Argon experienced field magnitude reductions of 3.0% and 5.5%, respectfully. At the $\frac{3}{4}$ cycle, Xenon and Argon experience field reductions of 2.4% and 9.7%, respectfully.

At the higher pressures, the variation between gas species become less pronounced. At 50 mTorr, Xenon showed 1.6% greater field magnitude at the $\frac{1}{4}$ cycle but 1.7% lower field magnitude at the $\frac{3}{4}$ cycle compared to Argon. 50 mTorr showed the least variation from the vacuum case at the $\frac{1}{4}$ cycle with Xenon having increased by 0.2% and Argon decreasing by 1.4%. Significant increases in field magnitude are still observed at the $\frac{3}{4}$ cycle with Xenon showing an increase of 17.4% and Argon an increase of 19.5%. However, compared to the 10 mTorr pre-fill, Xenon experiences a decrease of 8.4% and 13.1% at the $\frac{1}{4}$ and $\frac{3}{4}$ cycles, respectfully. Argon see similar reductions, 6.7% at the $\frac{1}{4}$ cycle and 12.3% at the $\frac{3}{4}$ cycle.

At 100 mTorr, the field magnitude of Xenon at the $\frac{1}{4}$ cycle exceeds Argon by 0.4% but shows a 6.2% deficit at the $\frac{3}{4}$ cycle. At the $\frac{1}{4}$ cycle, Xenon shows decreases of 1.7% and 10.1% relative to the vacuum test and 10 mTorr test, respectfully. Argon decreased 2.2% relative to vacuum and 7.4% relative to the 10 mTorr test. At the $\frac{3}{4}$ cycle, Xenon and Argon show increases of 4.5% and 11.0%, respectfully, over the vacuum test. Relative to the 10 mTorr test, Xenon and Argon show a 22.6% and 18.5%, respectfully, reductions of field magnitude. These results are tabulated in Table 1 for convenience.

Table 1: Percent difference of Argon and Xenon magnetic fields relative to vacuum and initial plasma test at 10 mTorr pre-fill. Negative values indicate a reduction in field magnitude from the reference test.

(a) Relative to vacuum

| Pressure | $\frac{1}{4}$ cycle | | $\frac{3}{4}$ cycle | |
|---|---|---|---|---|
| [mTorr] | Xenon | Argon | Xenon | Argon |
| 10 | 9.4 | 5.7 | 35.1 | 36.2 |
| 30 | 6.1 | -0.2 | 31.8 | 23.0 |
| 50 | 0.2 | -1.4 | 17.4 | 19.5 |
| 100 | -1.7 | -2.2 | 4.5 | 11.0 |

(b) Relative to 10 mTorr

| Pressure | $\frac{1}{4}$ cycle | | $\frac{3}{4}$ cycle | |
|---|---|---|---|---|
| [mTorr] | Xenon | Argon | Xenon | Argon |
| 30 | -3.0 | -5.5 | -2.4 | -9.7 |
| 50 | -8.4 | -6.7 | -13.1 | -12.3 |
| 100 | -10.1 | -7.4 | -22.6 | -18.5 |

## B. Energy Analysis

In an effort to quantify the effects of the circuit parameters on the early time formation physics of pulse inductive plasma, the distribution of the energy in MPX is calculated. Initially, all energy is stored in the MPX capacitor. After the discharge is initiated, current flows through the theta pinch coil storing energy in the magnetic field. For the analysis contained in this paper, it is assumed that the only energy loss mechanism present in the vacuum case is ohmic heating through a series resistance. The energy balance equation is given by

$$\frac{1}{2}CV_0^2 = \int_0^t I^2(\tau)Rd\tau + \frac{1}{2}CV^2(t) + \frac{1}{2}LI^2(t) + E(t)_{plasma} + E(t)_{other} \tag{4}$$

where $C$ is capacitance, $V$ is voltage, and $R$ is the series resistance. The first term in Eq. 4 is the energy loss to ohmic heating of the series resistance. The second term is the energy stored electrically in the capacitor. The third term is the energy stored in magnetic fields. The forth term is the energy deposited into the plasma. The final term is the energy not accounted for in the first four terms. To model the energy dynamics of MPX, a series RLC circuit is used. It is assumed that any stray capacitance will be small compared to the 0.707 $\mu$F capacitor capacitance. Determining the series resistance and inductance is a challenge. The addition of a spark gap plasma switch results in a series resistance and inductance that vary with time. Because ohmic heating is assumed to be the only loss mechanism, the time integral of the square of the current is divided by the initial energy stored on the capacitor to determine $R$. The resulting constant series resistance is 40 m$\Omega$. To determine the series inductance of the circuit, a least-squares estimate is performed over an iteration of inductance values. For the vacuum case, the series inductance is determined to be 183.3 nH. The resulting distribution of energy for the vacuum case is shown in Fig. 7.

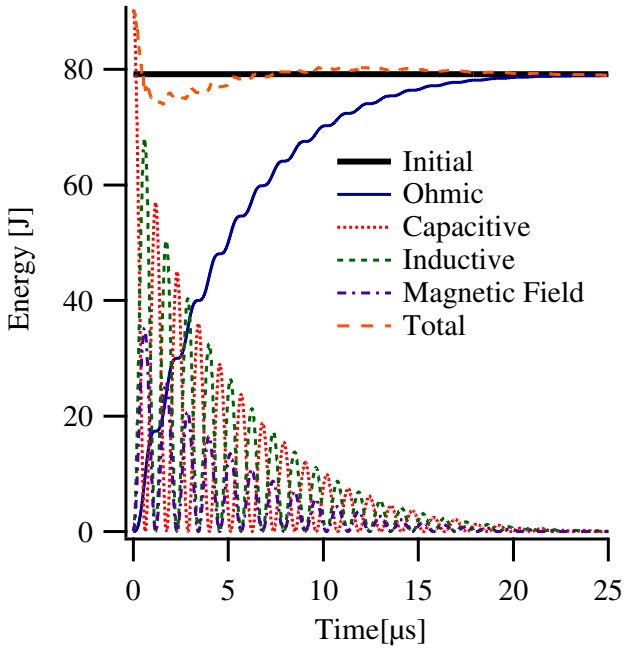


Figure 7: Vacuum energy analysis of MPX using series RLC values of 40.1 mΩ, 183.3 nH, and 0.707 $\mu$F.

The total energy is the sum of the ohmic loss, capacitive energy, and inductive energy at a given time. The energy associated with the magnetic field are also plotted but this is a subset of the inductive energy and is therefore not explicitly considered when calculating total energy. In the ideal case, the total energy should be equivalent to the initial energy stored on the capacitor. However, initial switching transients in the current monitor waveform resulted in an integration offset when calculating the voltage on the capacitor. This results in an energy that temporarily exceeds the initial energy stored in the system. Furthermore, the chosen values for the series resistance and impedance will result in deviations from the theoretical total energy. In the early discharge times, a LSE fit to the first quarter cycle yielded a series resistance and inductance of 24.0 mΩ and 202 nH, respectfully. These represent a 40.2% and 10.2%, respectfully, deviation from the assumed constant values. As illustrated in Fig. 2b, there is significant broadening observed in the frequency domain which is not captured in this model. Because averaged resistance and inductance values are used, portions of the total energy will fluctuate about the initial energy and will necessarily return to zero per the choice of $R$.

The energy associated with a magnetic field is given by

$$E_B = \frac{B^2}{2\mu_0} V, \tag{5}$$

where $V$ is the volume of the region of space where the field is present. To calculate the energy contained in the magnetic field of MPX, a cubic spline interpolation method was used to increase the spacial resolution from 6.72 cm to 0.01 cm. It is then assumed that the magnetic field magnitude is uniform the disc-shaped region of space under each probe. The energy is then calculated for each differential volume element which is then summed over the length of the coil. The peak energy calculated for the vacuum case using this approach is 35.2 J or 44.4% of the initial energy stored on the capacitor. However, using the Grover[20] handbook equations for inductance, a theoretical coil inductance of 36.24 nH is calculated. The total series inductance determined from the LSE analysis yielded a vacuum series inductance of 183.3 nH. The inductance calculated from Grover indicates that the theta pinch coil constitutes 21.8% of the total system inductance. This gives a theoretical maximum of 17.2 J of energy deposited into the MPX magnetic field. This is nearly half of the energy measured from the magnetic probes. One likely reason for the discrepancy is the segmented design of the MPX theta pinch coil. The Grover equations are not optimized for use on inductors with gaps between coil windings which can results in an error in the calculation of the magnetic field. The reduction of conducting material typically results in an increase in inductance; however, the segmented

design is technically eleven single inductors connected in a parallel configuration. In most applications, adding inductors in parallel reduces inductance. But due to the extreme proximity of the coil segments, the segments behave similar to a single solid coil.

In tests where plasma is present, the LSE yielded an average inductance of 166.4 nH for Argon and 166.8 nH for Xenon, a difference of 0.22%. An example of the energy distribution with plasma formation is illustrated in Fig. 8

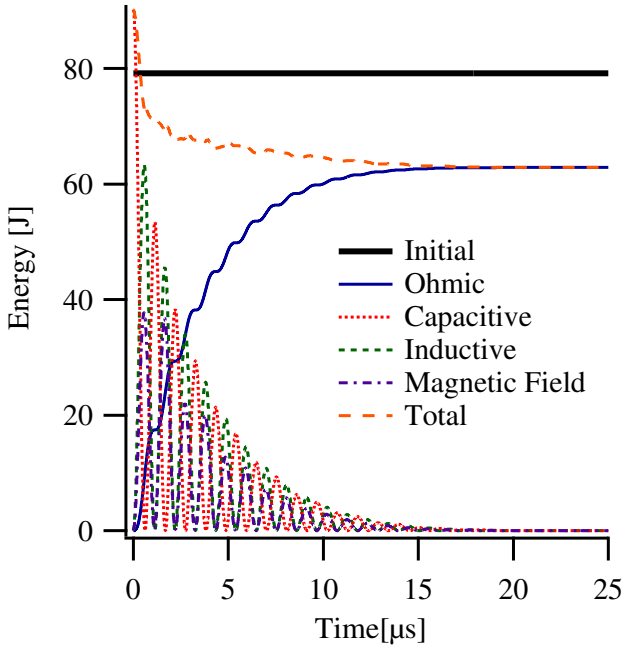


Figure 8: Plasma energy analysis of MPX using series RLC values of 40.1 mΩ, 166.1 nH, and 0.707 $\mu$F with a 10 mTorr Argon pre-fill.

A similar overshoot is observed in the early times due to trigger noise. For the plasma analysis, the same resistance is used as the DC resistance of the MPX circuit does not change due to the mutual inductance coupling with the plasma. The new inductance calculated for the plasma energy distribution combines the series inductance term with the mutual inductance term to gain a quantitative indication of the effect of plasma on the MPX circuit. The new inductance is 9.2% lower than the vacuum inductance. This variation in inductance would account for 3.3% of the 5.3% increase in discharge frequency. This indicates that the capacitance may be increasing by a maximum 3.1%. Furthermore, it is noticed that only 62.9 J of the total energy is accounted for. It is therefore assumed that this deficit in energy is due to the plasma presence. In the case of the 10 mTorr Argon pre-fill, 16.3 J has left the MPX circuit. The analysis of this missing energy with respect to plasma energy loss mechanisms (i.e., radiation, transport to wall, etc.) is the focus of a future publication. The magnetic field energy is also plotted for this test but based on earlier discussion of field aberrations resulting from plasma formation, the energy in the field cannot be accurately determine without knowing the geometry of the plasma.

The resulting energy deficits are plotted for Argon and Xenon in Fig. 9a and Fig. 9b, respectfully. The deficits show the effects of increase pre-fill pressure on total energy loss from the MPX circuit. Final deficit energy values are tabulated in Table 2 for convenience. Ideally the magnetic field returns to zero at the end of the test. However, due to random bit error during probe voltage integration, a small non-zero quantity is reported for the vacuum case of 0.23 J and 0.27 for Argon and Xenon, respectfully. Compared to 15.9 J, the smallest value observed during plasma tests, this non-zero value represents a maximum error of 1.7%. While the 0.04 J variation in the plasma cases appears to be significant, it is only 0.25% of the smallest observed energy, 15.9 J. The maximum disagreement between Argon and Xenon deficit energy is observed at 50 mTorr, but is a difference of only 6.9%. The energy deficits increase with time with Xenon showing a peak deficit of 21.6 J.

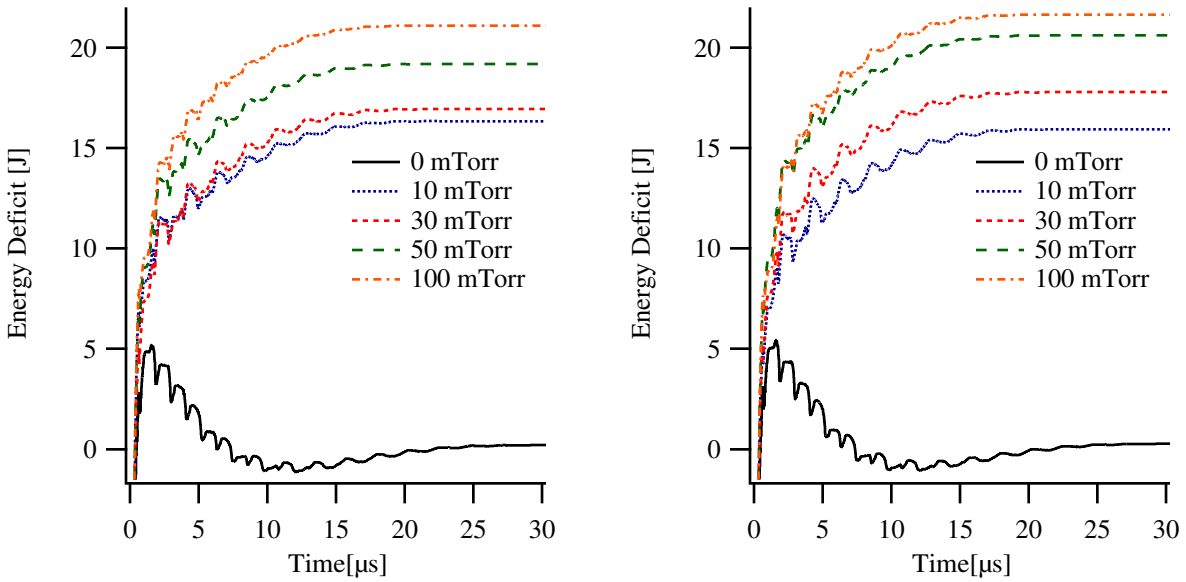


(a) Argon (b) Xenon

Figure 9: Energy deficit of Argon and Xenon at various pre-fill pressures.

Table 2: Energy deficit calculated from MPX circuit analysis for Argon and Xenon.

| Pressure | Energy Deficit [J] | |
|---|---|---|
| [mTorr] | Argon | Xenon |
| 0 | 0.23 | 0.27 |
| 10 | 16.3 | 15.9 |
| 30 | 16.9 | 17.8 |
| 50 | 19.2 | 20.6 |
| 100 | 21.1 | 21.6 |

## V. Conclusions

Current and magnetic field data for Argon and Xenon plasma are presented and combined with a RLC circuit analysis to determine the effects of plasma on the discharge circuit. It was observed that the presence of plasma resulted in a 5.9% increase in discharge frequency and an increase in the magnetic field magnitude of 36.2% near the wall of the quartz tube for the 10 mTorr pre-fill tests. Maximum field magnitude increases occurred after the first zero crossing of the current indicating significant plasma formation occurs between the first and third quarter cycles in agreement with the literature. Energy balance analysis show increased energy losses to the plasma with increasing pressure. A maximum of 21.6 J is deposited into Xenon at 100 mTorr, 27.2% of the initial energy stored in the system. The largest increase in energy occurred from vacuum to 10 mTorr. Further increases in pressure yielded 30.0% greater energy deposition into Argon and 35.8% into Xenon. This result indicates an optimum operating condition exists to maximize energy coupling to the plasma and reducing wasted propellant mass.

## Acknowledgments

*The authors of this paper would like to thank the Air Force Office of Scientific Research (grant FA9550-10-1-0204, grant monitor Dr. Mitat Birkan) for funding this research.*

# References


[1]Tuszewski, M., "Field Reversed Configurations," *Nuclear Fusion*, Vol. 28, No. 11, Nov. 1988, pp. 2033.

[2]Intrator, T., Park, J., Degnan, J., Furno, I., Grabowski, C., Hsu, S. C., Ruden, E., Sanchez, P. G., Taccetti, J., Tuszewski, M., Waganaar, W. J., Wurden, G., Zhang, S., and Wang, Z., "A High-Density Field Reversed Configuration Plasma for Magnetized Target Fusion," *IEEE Transactions on Plasma Science*, Vol. 32, No. 1, 2004, pp. 152–160.

[3]Armstrong, W. T., Linford, R. K., Lipson, J., Platts, D. A., and Sherwood, E. G., "FieldReversed Experiments (FRX) on Compact Toroids," *Physics of Fluids*, Vol. 24, No. 11, Nov. 1981, pp. 2068.

[4]Grabowski, C., Degnan, J., Amdahl, D., Delaney, R., Domonkos, M., Lehr, M., Magallanes, R., Robinson, R., Ruden, E., White, W., Gale, D., Kostora, M., McCullough, J., Sommars, W., Frese, M., Frese, S., Camacho, F., Coffey, S., Intrator, T., Wurden, G., Siemon, R., Fuelling, S., Bauer, B., Lynn, A., and Roderick, N., "FRC Lifetime Studies for the Field Reversed Configuration Heating Experiment," *53rd Annual Meeting of the APS Division of Plasma Physics*, Salt Lake City, UT, Nov. 2011.

[5]Kirtley, D., Brown, D. L., Gallimore, A. D., and Haas, J., "Details on an AFRL Field Reversed Configuration Plasma Device," Tech. rep., June 2005.

[6]Slough, J. T., Blair, A., Pihl, C., and Votroubek, G., "Magnetically Accelerated Plasmoid (MAP) Thruster - Initial Results and Future Plans," *30th International Electric Propulsion Conference*, Florence, Italy, Sept. 2007.

[7]Slough, J. T., Kirtley, D., and Weber, T., "Pulsed Plasmoid Propulsion: The ELF Thruster," *31th International Electric Propulsion Conference*, Ann Arbor, Michigan, Sept. 2009.

[8]Pahl, R. A. and Rovey, J. L., "Pre-Ionization Plasma in a FRC Test Article," *50th Aerospace Sciences Meeting*, Nashville, TN, Jan. 2012.

[9]Pahl, R. A., Rovey, J. L., and Pommerenke, D. J., "Calibration of Magnetic Field Probes at Relevant Magnitudes," *40th IEEE Conference on Plasma Science*, San Francisco, CA, June 2013.

[10]Carobbi, C. F. M., Millanta, L., and Chiosi, L., "The High-Frequency Behavior of the Shield in the Magnetic-Field Probes," *IEEE International Symposium on Electromagnetic Compatibility, 2000*, Vol. 1, 2000, pp. 35–40 vol.1.

[11]Loewenhardt, P., Blackwell, B., and Zhang, B., "A Simple Miniature Magnetic Probe with Inherent Electrostatic Rejection," *Review of Scientific Instruments*, Vol. 64, No. 11, 1993, pp. 3334–3335.

[12]Shaw, R. S., Booske, J., and McCarrick, M. J., "Broadband Calibration for Magnetic Probes for use in the Maryland Spheromak," *Review of Scientific Instruments*, Vol. 58, No. 7, 1987, pp. 1204–1210.

[13]Messer, S., Blackwell, D. D., Amatucci, W. E., and Walker, D. N., "Broadband Calibration of Radio-Frequency Magnetic Induction Probes," *Review of Scientific Instruments*, Vol. 77, No. 11, Nov. 2006, pp. 115104.

[14]Bronaugh, E., "Helmholtz Coils for Calibration of Probes and Sensors: Limits of Magnetic Field Accuracy and Uniformity," *, 1995 IEEE International Symposium on Electromagnetic Compatibility, 1995. Symposium Record*, 1995, pp. 72–76.

[15]*IEEE Standard 1309-2005 for Calibration of Electromagnetic Field Sensors and Probes, Excluding Antennas, from 9 kHz to 40 GHz*, IEEE Electromagnetic Compatibility Society, New York, Dec. 2005.

[16]Franck, C., Grulke, O., and Klinger, T., "Magnetic Fluctuation Probe Design and Capacitive Pickup Rejection," *Review of Scientific Instruments*, Vol. 73, No. 11, 2002, pp. 3768–3771.

[17]Carobbi, C. F. M. and Millanta, L., "Analysis of the Common-Mode Rejection in the Measurement and Generation of Magnetic Fields using Loop Probes," *IEEE Transactions on Instrumentation and Measurement*, Vol. 53, No. 2, 2004, pp. 514–523.

[18]Hill, C. S., *Translation Studies on an Annular Field Reversed Configuration Device for Space Propulsion*, Dissertation, Michigan Technological University, 2012.

[19]Meeks, W. C. and Rovey, J. L., "On the Delayed Gas Breakdown in a Ringing Theta-Pinch with Bias Magnetic Field," *Physics of Plasmas*, Vol. 19, No. 5, May 2012, pp. 052505.

[20]Grover, F., *Inductance Calculations: Working Formulas and Tables*, Dover Publications, Van Nostrand, New York, 1946.